Chemical Science

ROYAL SOCIETY OF CHEMISTRY

EDGE ARTICLE

View Article Online
View Journal | View Issue

Cite this: *Chem. Sci.*, 2025, **16**, 7387

All publication charges for this article have been paid for by the Royal Society of Chemistry

Received 31st December 2024
Accepted 19th March 2025

DOI: 10.1039/d4sc08815h

rsc.li/chemical-science

Rearranging spin electrons by axial-ligand-induced hybridization state transition to boost the activity of nickel single-atom-catalysts for electrochemical CO_2 reduction†

Mingxia Peng,[a] Kai Huang,[b] Xiuyuan Hu,[c] Andrea Zitolo,[d] Honglai Liu,[ae] Cheng Lian *[ae] and Jingkun Li *[a]

Single-atom catalysts (SACs) with M–N_4 active sites show great potential to catalyze the electrochemical CO_2 reduction reaction (eCO_2RR) toward CO. The activity and selectivity of SACs are determined by the local coordination configuration of central metal atoms in M–N_4 sites, which is readily tuned by axial ligands. In this work, we construct axial ligands *in situ* on two Ni–N_4-type model SACs, NiPc and Ni–N–C, by adding Cl^- into the electrolyte taking advantage of the strong chemisorption of Cl^- over Ni–N_4. Cl axial ligand lowers the energy barrier of the potential-determining step for the eCO_2RR due to a hybridization state transition of Ni orbitals and the resulting rearrangement of spin electrons. Consequently, both NiPc and Ni–N–C with axial Cl exhibit superior activity for the eCO_2RR toward CO. Finally, we propose the magnetic moment of Ni as a universal descriptor for the eCO_2RR toward CO on Ni–N_4 with various axial ligands.

Introduction

The electrochemical CO_2 reduction reaction (eCO_2RR) yielding value-added chemicals and fuels, coupled with renewable electricity, offers a sustainable solution to achieve carbon neutrality.[1] The products of the CO_2RR vary from C1 (CO, CH_4, HCOOH, CH_3OH, *etc.*) to C2+ (CH_3CH_2OH, C_2H_4, *etc.*).[2] The high energy barrier for C–C coupling, which is the key step to form C2+ products, generally leads to high overpotential and low selectivity for the eCO_2RR toward C2+.[3] In contrast, C1 products with fewer electrons transferred (*e.g.*, CO and HCOOH) are economically favorable due to their low overpotential,[3] high selectivity, and enhanced energy efficiency.[4] CO constitutes a crucial raw material in industrial production processes.[5] Particularly, CO and H_2 (the by-product of the eCO_2RR) with a tunable ratio co-produced by the eCO_2RR can be readily used as a feedstock for syngas.[6] In addition, cascade eCO_2RR systems, which integrate two consecutive steps of CO_2-to-CO and CO-to-C2+ either within one CO_2 electrolyzer using a bifunctional cathode or in two tandem CO_2 and CO electrolyzers,[7–9] have been reported to boost the current density and faradaic efficiency (FE) for the eCO_2RR toward C2+. Thus, extensive efforts have been devoted to exploring catalysts for the eCO_2RR toward CO with outstanding activity and tunable selectivity in the past decades.[10,11]

Single-atom catalysts (SACs) with unique electronic and geometric structures exhibit superior activity and selectivity for the eCO_2RR toward CO.[12,13] The M–N_4 (M = Fe, Co, Ni, Cu, *etc.*) moieties, in both macrocyclic metal complexes (metal porphyrins, metal phthalocyanines (MPc), *etc.*) and their analogous metal–nitrogen–carbon (M–N–C) materials, are widely accepted as active sites.[14,15] Particularly, nickel SACs deliver extraordinary performance with a FE >90% at a wide potential range.[16,17] However, nickel SACs still suffer from insufficient activity in practical CO_2 electrolyzers, leading to a significantly reduced selectivity of the eCO_2RR toward CO at high current densities (*e.g.*, >200 mA cm^{-2}).[17] Thus, it is pivotal to further boost the activity of Ni SACs for the eCO_2RR toward CO to promote their feasible implementation in large-scale CO_2 electrolyzers. It is reported that the symmetric D_{4h} square-planar geometry of Ni–N_4 is unfavorable for adjusting the spatial distribution of electrons and, consequently impedes the electron transfer during electrochemical reactions.[17–20] Hence, breaking the D_{4h} symmetry of Ni–N_4 *via* geometric distortion modulates their

[a]*School of Chemistry and Molecular Engineering, East China University of Science and Technology, Shanghai 200237, P. R. China. E-mail: liancheng@ecust.edu.cn; lijingkun@ecust.edu.cn*

[b]*School of Pharmaceutical and Chemical Engineering, Taizhou University, Taizhou, Zhejiang, 318000, P. R. China*

[c]*No. 2 High School of East China Normal University, 555 Chenhui Rd, Pudong, Shanghai, 201203, P. R. China*

[d]*Synchrotron SOLEIL, L'Orme des Merisiers, Départementale 128, 91190 Saint-Aubin, France*

[e]*State Key Laboratory of Chemical Engineering, East China University of Science and Technology, Shanghai 200237, P. R. China*

† Electronic supplementary information (ESI) available. See DOI: https://doi.org/10.1039/d4sc08815h

electronic structures, leading to accelerated electron transfer and enhanced activity of nickel SACs for the eCO_2RR toward CO.[21]

Regulating the planar and axial ligands are two major strategies for tuning the geometric and electronic structures of M–N_4.[22–25] Planar ligand regulation includes doping with heteroatoms,[26,27] engineering surface vacancies,[28,29] adjusting coordination numbers,[30] and constructing multi-atom sites.[6] For example, S. Ji *et al.*[31] incorporated P heteroatoms in the second coordination shell of Fe–N_4 to break the local symmetry of electron distribution, leading to excellent activity and stability for oxygen reduction and evolution reactions. S. Chen *et al.*[32] doped sulfur in the second coordination shell of Fe–N_4, which induces a pronounced proton-feeding effect to boost the eCO_2RR. However, it remains a great challenge for the precise and site-specific manipulation of the first and/or secondary coordination shell of central metal atoms, resulting in heterogeneous structures of planar coordination particularly for M–N–Cs obtained by high-temperature pyrolysis.[33,34] In contrast, M–N_4 sites with axial ligands constitute a well-defined proximal coordination configuration with tunable geometric and electronic structures.[22] M. Li *et al.*[35] reported an electronic localization enhancement of Ni–N_4 induced by the Cl axial ligand, accounting for the superior HER activity of Ni–N_4–Cl. However, electronic-level insights into the axial effect in tuning the eCO_2RR activity of M–N_4 moieties are still lacking, which is crucial for designing highly efficient SACs for the eCO_2RR.

Herein, we systematically investigated the electronic structures and eCO_2RR activities of two Ni–N_4-type model SACs, namely NiPc and Ni–N–C, with and without the axial ligand. The axial ligand is introduced *in situ* by adding Cl^- into the electrolyte taking advantage of the strong chemisorption of Cl^- on Ni–N_4. The Cl axial ligand induces a transition in hybridization states of Ni orbitals and a rearrangement of spin electrons, leading to the low energy barrier for the formation of key intermediate COOH*. As a result, Ni–N_4 SACs with Cl axial ligands exhibit an enhanced CO partial current density. The magnetic moment of Ni is proposed as a universal descriptor for the eCO_2RR toward CO on Ni–N_4 with various axial ligands. This study provides a feasible strategy for screening highly efficient M–N_4-type SACs with axial ligands for the eCO_2RR toward CO.

Results and discussion

There are two typical classes of SACs extensively investigated for the eCO_2RR: macrocyclic metal complexes (*e.g.*, MPc) with a well-defined square-planar M–N_4 coordination configuration[36] and their analogous M–N–Cs consisting of isolated metal atoms anchored on nitrogen-doped carbon.[37] M–N–Cs derived from high-temperature pyrolysis generally show heterogeneous structures, with well-recognized structures of bulk-hosted M–N_4–C_{10} moieties embedded within a graphene sheet (denoted as MN_4 hereafter) and edge-hosted M–N_{2+2}–C_{4+4} bridging two adjacent graphene sheets (denoted as MN_{2+2} hereafter).[38–40] Taking into consideration the superior activity and selectivity of Ni–N_4 moieties,[17,36] we focus on Ni SACs and exploit NiPc, NiN_4 and NiN_{2+2} as representative model structures (Fig. 1a–c) to investigate the effect of axial ligands on their electrocatalytic activity for the eCO_2RR toward CO *via* density functional theory (DFT) simulations.

We then utilized NiPc and Ni–N–C as model catalysts to verify the positive effect of Cl axial ligand on the electrolytic activity of Ni–N_4 for the eCO_2RR toward CO. NiPc was loaded on carbon supports *via* ball milling to enhance the electronic conductivity, followed by a heat treatment under milder conditions (300 °C) to stabilize NiPc on carbon without altering its structure.[41,42] A Ni–N–C material consisting of atomically dispersed nickel sites was synthesized according to our previous work.[43] The X-ray diffraction (XRD) pattern of Ni–N–C reveals two characteristic peaks of disordered carbon (Fig. S1a†), and the defective structure of carbon is further supported by the high intensity of D band at 1350 cm^{-1} in the Raman spectrum (Fig. S1b†). The scanning electron microscopy (SEM) image indicates a porous structure of Ni–N–C (Fig. 1d), which consists of abundant micropores and mesopores (Fig. S1c and d†). The Brunauer–Emmett–Teller surface area of Ni–N–C is 223 $m^2\ g^{-1}$ (Table S1†). The highly microporous and defective structure of the carbon matrix is favorable to anchor single atoms of transition metals.[44] The energy-dispersive X-ray spectroscopy (EDX) mappings show a uniform distribution of Ni, N, and C elements in Ni–N–C (Fig. 1e). No metallic particle is observed after an extensive evaluation of high-angle annular dark-field scanning transmission electron microscopy (HAADF-STEM) images (Fig. 1f), in good agreement with the absence of characteristic peaks arising from nickel-based agglomerates in XRD (Fig. S1a†). The isolated nickel atoms are distinctly visible (highlighted by red circles) in the abbreviation-corrected STEM image (Fig. 1g), confirming that nickel in Ni–N–C is present as single atoms.

The atomically dispersed nature of nickel in Ni–N–C is further supported by X-ray absorption spectroscopy (XAS) and X-ray photoelectron spectroscopy (XPS) (Fig. 1h–l). The Ni 2p X-ray photoelectron spectroscopy (XPS) spectrum of Ni–N–C delivers only one main peak arising from Ni^{2+} accompanied by several satellite peaks, and Ni^0 species is not detected (Fig. 1i).[45] The XANES spectrum of Ni–N–C significantly deviates from that of NiO (Fig. 1h), suggesting that the Ni^{2+} species detected in XPS is not in the form of oxide. Meanwhile, the Fourier transform of extended X-ray absorption fine structure (EXAFS) exhibits negligible signals at ~2.1 and ~2.4 Å attributed to the Ni–Ni backscattering in metallic nickel and nickel oxide (Fig. 1j and S3†), indicating the absence of nickel-based agglomerates. Thus, XPS, EXAFS, XRD and STEM characterization studies unambiguously demonstrate the atomic dispersion of nickel in Ni–N–C. The nickel content in Ni–N–C is 0.22 at% according to XPS (Table S2†).

Then we elucidate the coordination environment of atomically dispersed nickel sites in Ni–N–C with detailed analysis of N 1s XPS and EXAFS spectra. Five nitrogen species are identified in the N 1s XPS spectrum of Ni–N–C, namely, N in M–N_x, pyrrolic N (labeled as N–H), pyridinic N, graphitic N (including N_{gr} and N^+), and N–O_x (Fig. 1k and Table S3†).[43] The presence of abundant M–N_x suggests that nickel coordinates with nitrogen defects in the carbon matrix. Thus, we fit the Fourier transform

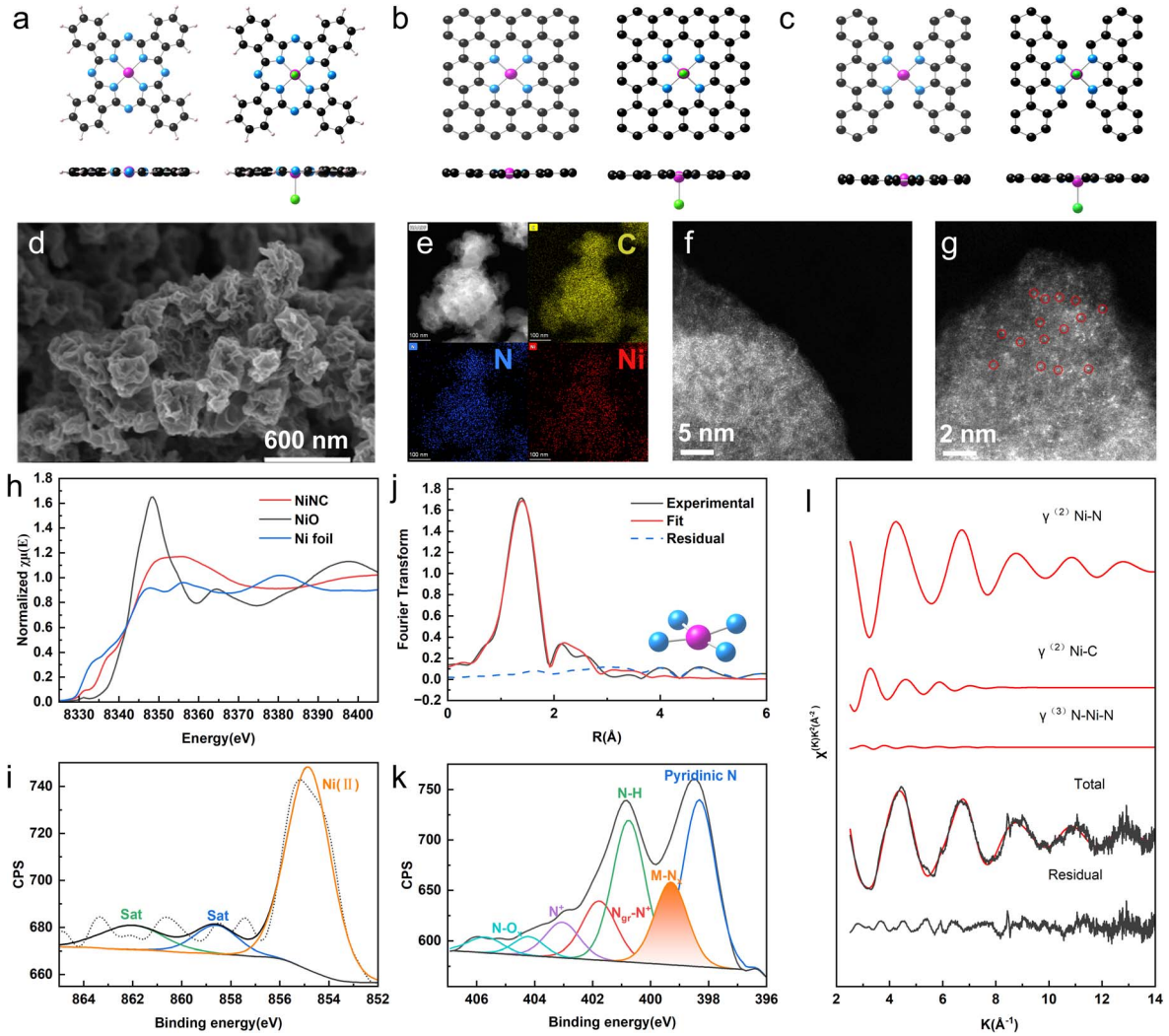

Fig. 1 The morphology and structure of Ni–N–C. Top views (upper panel) and side views (lower panel) of model structures for (a) NiPc, (b) NiN_4 and (c) NiN_{2+2} with and without Cl axial ligand. The black, blue, purple, green, and white balls represent C, N, Ni, Cl, and H atoms, respectively. (d) SEM image. (e) HAADF-STEM image and the corresponding EDX mappings. (f and g) Abbreviation-corrected STEM images with different magnifications. (h) Ni K-edge XANES spectrum. The spectra for nickel foil and nickel oxide powders are also presented as references. (i) Ni 2p XPS spectrum. (j) The Fourier transform of experimental and best fit Ni K-edge EXAFS spectra. Inset is the schematic model for the best fit, with nickel and nitrogen atoms represented by purple and blue balls, respectively. No phase-shift correction was applied to the Fourier transforms. (k) N 1s XPS spectrum. (l) Ni K-edge EXAFS analysis: Ni–N, Ni–C $\gamma(2)$ two-body signals and the N–Ni–N $\gamma(3)$ three-body signal included in the fit, the total signal (red line) superimposed on the experimental one (black line).

of the experimental EXAFS spectrum of Ni–N–C with a variable number of in-plane nitrogen atoms binding the Ni^{2+} center (inset of Fig. 1j), and the best-fit result shows a coordination number of 4.3 and a Ni–N bond distance of 1.92 Å (Table S4†). The dominant contribution is given by Ni–N first shell coordination (Fig. 1l), leading to the major peak at 1.5 Å in the Fourier transform of the EXAFS spectrum (Fig. 1j). In contrast, Ni–C second shell coordination contributes to the minor peak in the range of 2–3 Å (Fig. 1j and l).[40] The intensity of the N–Ni–N signal is insufficient to determine the bond angle and, consequently, the geometric structure of the Ni–N_4 moiety. Therefore, the nickel single atoms in Ni–N–C are mainly present in the form of Ni–N_4 moieties, with either square-planar or distorted geometry.

The eCO_2RR toward CO undergoes four elementary steps (written for acidic solutions): (1) $CO_2(g) + * \rightarrow CO_2*$, (2) $CO_2* + H^+ + e^- \rightarrow COOH*$, (3) $COOH* + H^+ + e^- \rightarrow CO* + H_2O(g)$, and (4) $CO* \rightarrow CO(g) + *$,[46] with a debatable potential-determining step (PDS) of either COOH* formation or CO_2* adsorption.[46,47] The configurations of all elementary steps on NiPc, NiN_4 and NiN_{2+2} models are shown in Fig. S3.† The free energy (G) diagrams for the eCO_2RR toward CO over three models show that the Gibbs free energy change (ΔG) of COOH* formation is the highest among four elementary steps (Fig. 2a–c and Table S5†). Thus, we can infer that the first proton coupled electron transfer to form COOH* is the potential-determining step (PDS) for the eCO_2RR toward CO over Ni–N_4. The changing current densities with pH on an absolute scale (*vs.* normal hydrogen

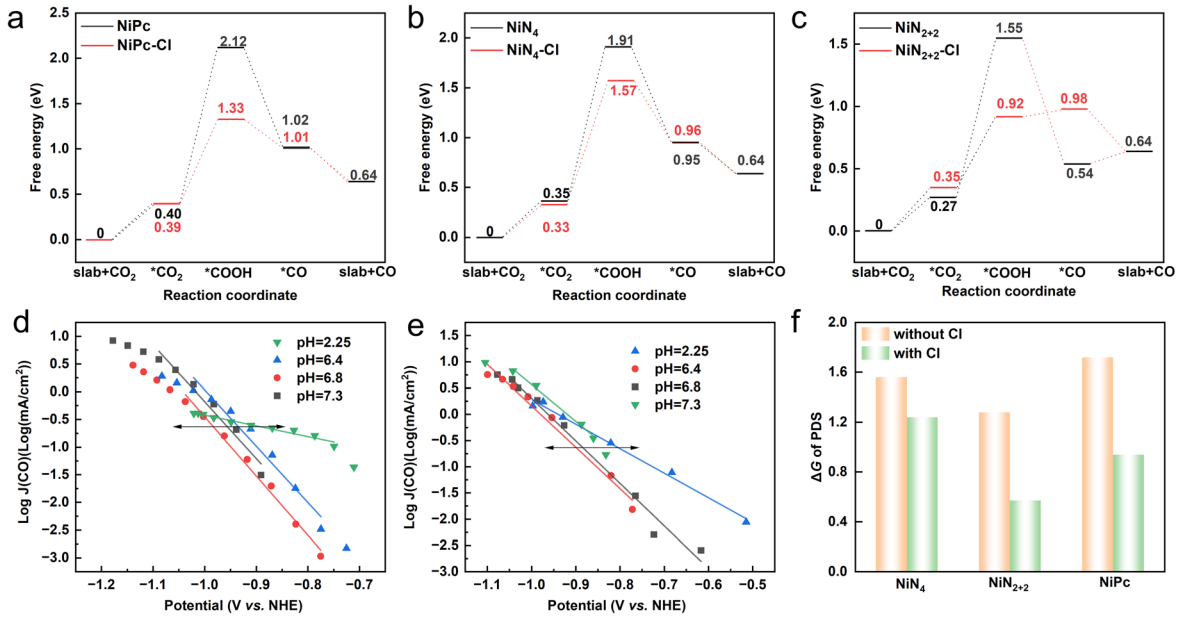

Fig. 2 The effect of Cl axial ligand on the energy barrier of PDS for the eCO_2RR toward CO over Ni–N_4. Free energy diagrams of the eCO_2RR to CO for (a) NiPc, (b) NiN_4 and (c) NiN_{2+2} with and without the Cl axial ligand. Experimental current densities plotted against potential *vs.* NHE for (d) NiPc and (e) Ni–N–C. (f) Comparison of the ΔG of PDS for NiPc, NiN_4 and NiN_{2+2} with and without the Cl axial ligand.

electrode (NHE)) over NiPc and Ni–N–C (with NiN_4 and NiN_{2+2} structures) indicate that proton participates in the PDS (Fig. 2d and e), further confirming COOH* formation as PDS for the eCO_2RR toward CO. Pinpointing Cl axial ligand on Ni–N_4 does not alter the PDS (Fig. 2a–c), but lowers its energy barrier for all three model structures (Fig. 2f). Moreover, NiN_{2+2} exhibits the lowest ΔG among three models without the axial ligand due to the strong adsorption of *COOH. However, the strong adsorption of *CO over NiN_{2+2} as a consequence of linear scaling relationship[48] leads to an uphill *CO desorption ($\Delta G > 0$), in contrast to the spontaneous *CO desorption over Ni–N_4 and NiPc ($\Delta G < 0$). Interestingly, Cl axial ligand not only strengthens *COOH adsorption over NiN_{2+2}, but also weakens the adsorption of *CO, leading to a reduced energy barrier of PDS and a downhill *CO desorption. Thus, Cl axial ligand breaks the linear scaling relationship over NiN_{2+2},[48] probably due to the synergistic effect of the axial ligand and defects in the edges. Overall, the Cl axial ligand lowers the energy barrier of PDS for the eCO_2RR toward CO over Ni–N_4, boosting the catalytic activity of Ni single atoms.

We then measured the activity and selectivity of the eCO_2RR toward CO over NiPc and Ni–N–C, and evaluated the effect of Cl axial ligand by adding KCl in the electrolyte. The metal center in the M–N_4 site tends to be occupied by a H_2O molecule in the backside axial position,[49–51] and Cl^- in the electrolyte replaces H_2O due to the significantly higher binding energy of Cl than that of H_2O adsorbed on Ni–N_4 (including NiPc, NiN_4 and NiN_{2+2}) according to DFT simulations (Fig. 3a–c). Further charge analysis shows that Cl atoms transfer 0.14–0.15$|e|$ charges to Ni atoms, indicative of a strong chemisorption of Cl on Ni–N_4 (insets of Fig. 3a–c). In contrast, the charge transfer from H_2O molecules to Ni atoms is only 0.00–0.03$|e|$, suggesting a physisorption of H_2O on Ni–N_4 (insets of Fig. 3a–c). Thus, we can infer that Ni–N_4 binds with the Cl axial ligand by simply adding Cl^- in the electrolyte.

The CO and H_2 partial current densities *vs.* potential (*iR*-corrected) over NiPc and Ni–N–C catalysts in electrolytes measured in 1 M $KHCO_3$ electrolyte with 0, 10 and 100 mM KCl are presented in Fig. 3d–g. CO_2 electrolysis was conducted for 30 minutes at constant current densities from 10 mA cm^{-2} to 60 mA cm^{-2} in a flow cell with Ag/AgCl as the reference electrode. The total faradaic efficiencies (FEs) of CO and H_2 for NiPc and Ni–N–C are ~100% (Fig. S4†), indicating negligible liquid products formed during the eCO_2RR. Thus, we didn't measure liquid products for this study. Both NiPc and Ni–N–C exhibit enhanced CO partial current densities in a wide potential range after adding trace amount of Cl^- (10 mM), and the enhancement increases with an increasing Cl^- concentration (Fig. 3d and e). The improvement in the catalytic activity of Ni–N_4 for the eCO_2RR toward CO induced by the Cl axial ligand is consistent with the reduced energy barrier of PDS (Fig. 2a–c). In contrast, the H_2 partial current densities of NiPc and Ni–N–C are not affected by the addition of Cl^- (Fig. 3f and g). The above results demonstrate that the Cl axial ligand enhances the intrinsic activity of Ni–N_4 for the eCO_2RR toward CO without altering its HER activity, leading to an increase in the total current density (Fig. S5†). Moreover, during the 8-hour chronoamperometry (CA) tests in 1 M $KHCO_3$ electrolyte with 100 mM KCl, both Ni–N–C and NiPc maintained stable CO faradaic efficiency (FE) and current density, as shown in Fig. S6.† The Cl 2p spectra of the Ni–N–C and NiPc after stability tests exhibit a characteristic peak at ~198.0 eV attributed to Ni–Cl species (Fig. S7†),[52] with Cl as the axial ligand considering the absence of high-temperature required to form planar coordinated Cl.[24] In addition, a new

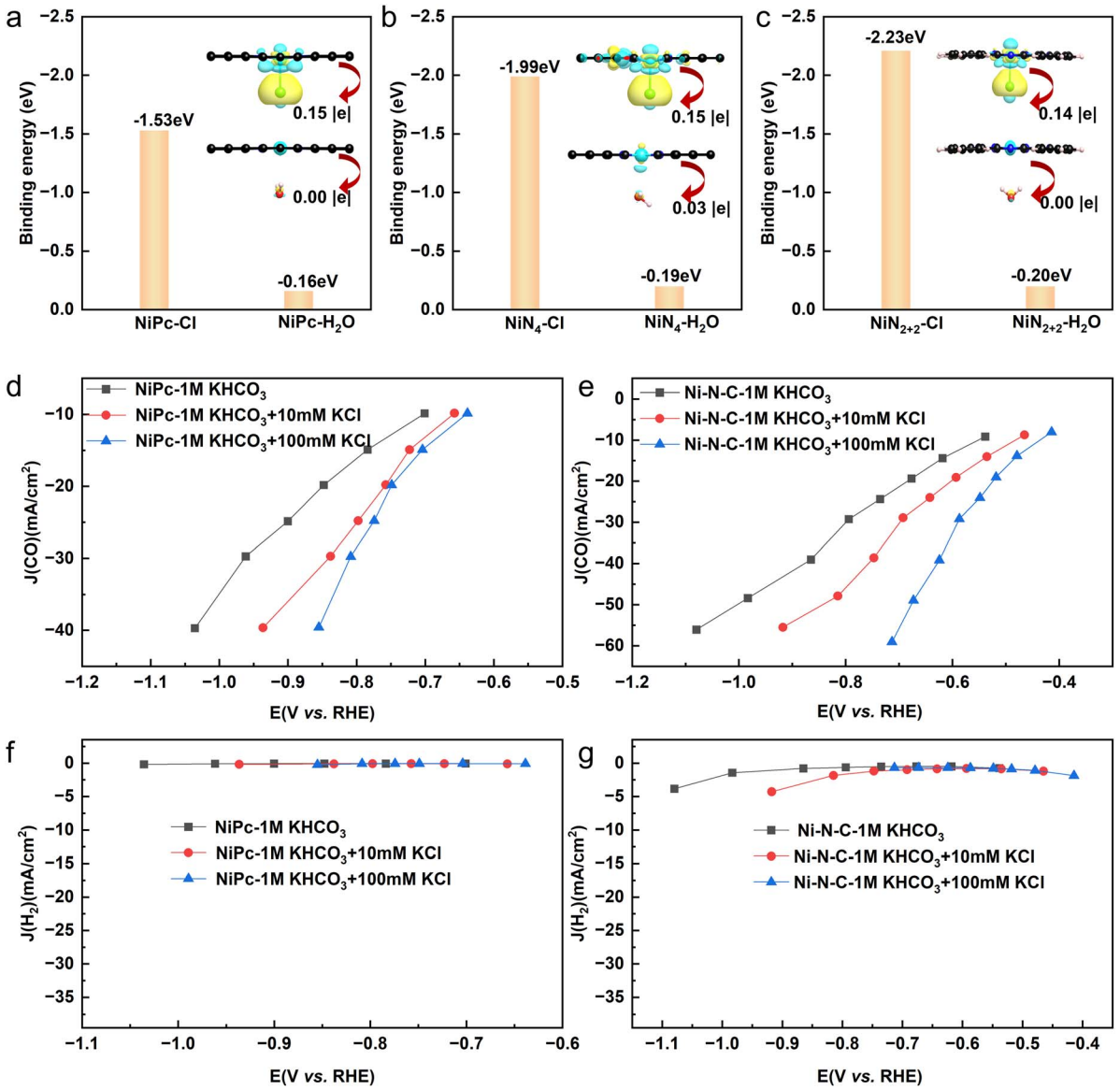

Fig. 3 The effect of Cl axial ligand on the activity of Ni–N_4 for the eCO_2RR toward CO. The binding energies of Cl and H_2O adsorbed on the Ni center in (a) NiPc, (b) NiN_4, and (c) NiN_{2+2}. The insets are the charge density differences of Cl and H_2O on Ni–N_4 sites. The cyan and yellow regions represent loss and accumulation of charge density, respectively, and the isosurface value is ±0.002 e $bohr^{-3}$. CO partial current densities *vs.* potential (*iR*-corrected) for (d) NiPc and (e) Ni–N–C. H_2 partial current densities *vs.* potential (*iR*-corrected) for (f) NiPc and (g) Ni–N–C. The above electrochemical characterization is measured in 1 M $KHCO_3$ electrolyte with 0, 10 and 100 mM KCl (the data shown in (d–g) are the average of three repeated experiments).

peak at 858.3 eV assigned to Ni^{3+} emerges in the Ni 2p XPS spectra of Ni–N–C and NiPc after stability tests (Fig. S8†), further confirming the formation of Ni–N_4–Cl with Cl as the axial ligand.[53] The postmortem XPS studies unambiguously demonstrate the successful introduction and high stability of the Cl axial ligand. Approximately 37% and 18% of Ni^{3+} species are detected in Ni–N–C and NiPc after the stability tests (Fig. S8†), suggesting that Ni–N_4 is partially coordinated with axial Cl ligands.

Strong chemisorption of the axial ligand on M–N_4 sites pulls single metal atoms away from the carbon plane, which breaks the D_{4h} symmetry of square-planar M–N_4, and consequently promotes the electron transfer during electrochemical reactions.[19,20] The distance of Ni atom from the carbon plane (d_{Ni}) and the Ni–N bond distance (d_{Ni-N}) (insets in Fig. 4a and b) describe the degree of geometric distortion of Ni–N_4 sites upon adsorption of Cl axial ligand. Thus, we explore the relationship between the energy barrier of PDS (ΔG_p) for the eCO_2RR and d_{Ni}/d_{Ni-N} (Fig. 4a and b). For comparison, weak adsorption of H_2O axial ligand on three models are considered (Fig. S9, S10 and Table S6†). In contrast to H_2O molecules (d_{Ni} = 0.02–0.08 Å), Cl atom with a strong binding energy on Ni–N_4 pulls Ni atom further away from the carbon plane (d_{Ni} = 0.10–0.33 Å), resulting in a larger d_{Ni-N} (Fig. 4a, b and Table S7†). There is a positive

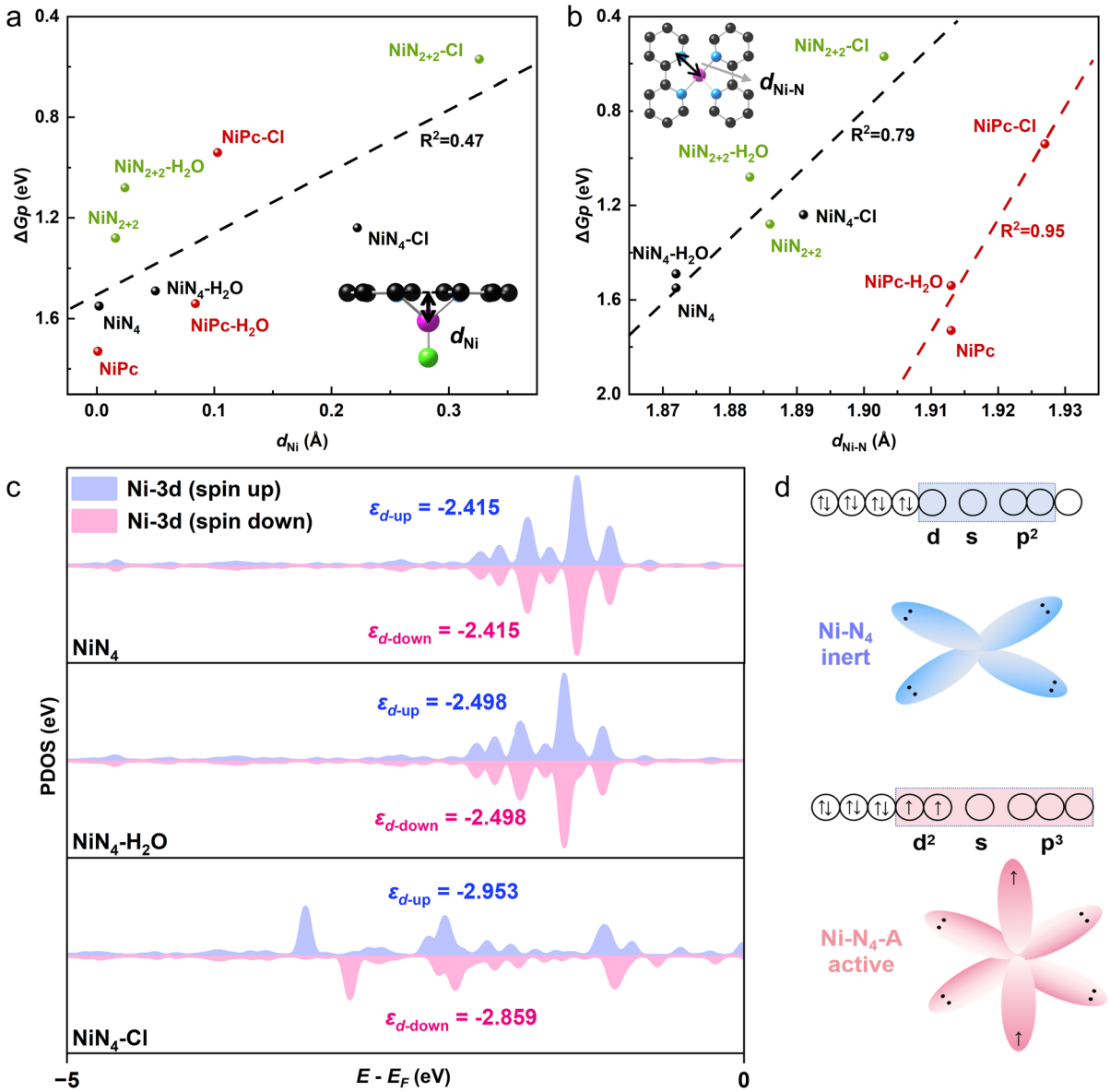

Fig. 4 The effect of Cl axial ligand on the geometric and electronic structure of Ni–N_4. The relationship between ΔG_p and (a) d_{Ni}, (b) d_{Ni-N}. (c) The partial density of states and d-band center of Ni atoms in NiN_4, NiN_4–Cl, and NiN_4–H_2O. (d) Schematic diagram of orbital hybridization of Ni atoms in Ni–N_4 with and without axial ligands.

correlation between d_{Ni} and ΔG_p: the further away the Ni atoms are from the carbon plane, the lower the ΔG_p (Fig. 4a). The relationship between d_{Ni-N} and ΔG_p falls into two linear lines for NiPc and Ni–N–C (NiN_4 and NiN_{2+2}), respectively (Fig. 4b). It is noteworthy that both the change of d_{Ni} and d_{Ni-N} of NiPc–Cl are smaller than those of NiN_4–Cl and NiN_{2+2}–Cl due to the more rigid structure of NiPc (Fig. 4a and b). Moreover, the periodic boundary conditions on the *xy* plane of molecular NiPc and periodic NiN_4/NiN_{2+2} are different for DFT simulations. Thus, it is reasonable that the linear coefficient for the correlation between the geometric parameters and ΔG_p of NiPc differs from that of Ni–N–C. In summary, Cl axial ligand induces geometric distortion of Ni–N_4 sites, and the geometric parameters, d_{Ni} and d_{Ni-N}, are strongly correlated with the energy barrier of PDS, and consequently the electrocatalytic activity for the eCO_2RR toward CO.

Then we evaluate the effect of Cl axial ligand on the electronic structures of Ni atoms in Ni–N_4. The partial density of states (PDOS) show that the up and down spin images of Ni 3d orbitals of NiN_4 and NiPc (with/without H_2O ligands) are symmetrical (Fig. 4c and S11a†), indicating the symmetrical arrangement of the up and down spin electrons of 3d orbitals for Ni–N_4 without geometric distortion (Fig. 4d). In contrast, the geometric distortion induced by Cl axial ligand results in the asymmetric up and down spin electron arrangement of Ni 3d orbitals, and thus the magnetic properties of NiN_4–Cl (Fig. 4c, d and S11a†). The empty 3d, 4s and two 4p orbitals of Ni undergo dsp^2 hybridization to interact with the sp^2 orbitals of

the four-coordinated N ligands in Ni–N_4 with square planar geometry,[54] whereas Ni–N_4 with Cl axial ligand exhibits a d^2sp^3 hybridization with an octahedral coordination environment (Fig. 4d). The d^2sp^3 hybridization of Ni leads to the rearrangement of spin electrons, which activates Ni–N_4 sites and boosts their intrinsic activity for the eCO_2RR.[54] Particularly, the up and down spin PDOS image of Ni 3d orbitals in NiN_{2+2} is asymmetric (Fig. S11b†), leading to a lower energy barrier for PDS of NiN_{2+2} than those of NiPc and NiN_4 (Fig. 2f). The Cl axial ligand further intensifies the degree of asymmetry for the PDOS image of Ni 3d orbitals in NiN_{2+2} (Fig. S11b†), indicating the enhanced activity of NiN_{2+2}–Cl for the eCO_2RR toward CO.

We then analyzed the d-electron distribution of Ni atoms in NiPc, NiN_4 and NiN_{2+2} with/without the Cl axial ligand (Fig. S12†). For all three models without Cl axial ligand, the peak of partial density of states (PDOS) below the Fermi level is mainly contributed by the d orbital components containing the *z*-axis direction (such as d_{yz}, d_{xz}, and d_{z^2}), indicating that the electrons involved in the eCO_2RR are mainly provided by the d orbitals in the *z*-direction. Stronger the electron donating capability of d orbitals, better the eCO_2RR activity we achieve. NiPc only provides electrons through d_{z^2} and d_{xz}, while all the d_{yz}, d_{xz}, and d_{z^2} of NiN_4 donate electrons. Moreover, the structural symmetry of NiN_{2+2} has been disrupted, enabling d_{xy} to donate electrons in addition to d_{yz}, d_{xz}, and d_{z^2}. The above results are in good agreement with the superior eCO_2RR activity of Ni–N–C to that of NiPc. Introducing Cl axial ligands further breaks the structural symmetry of NiPc, NiN_4 and NiN_{2+2}, which not only leads to asymmetric up and down spin images, but also brings the peak of d orbital components containing the *z*-axis direction closer to the Fermi level (Fig. S12†). As a result, the introduction of Cl axial ligands induces the strong electron donating capability and, consequently, enhances the eCO_2RR activity of Ni–N_4.

Since the asymmetric up and down spin electron arrangements of Ni 3d orbitals in Ni–N_4–Cl are crucial for their enhanced eCO_2RR activity, we then explore the relationship between ΔG_p and $\Delta\varepsilon_d$ (the difference in the d-band center of Ni between down and up spin). $\Delta\varepsilon_d$ delivers a good linear relationship with ΔG_p (Fig. S13a†). The change of $\Delta\varepsilon_d$ induced by Cl axial ligands for three model structures follows the trend of

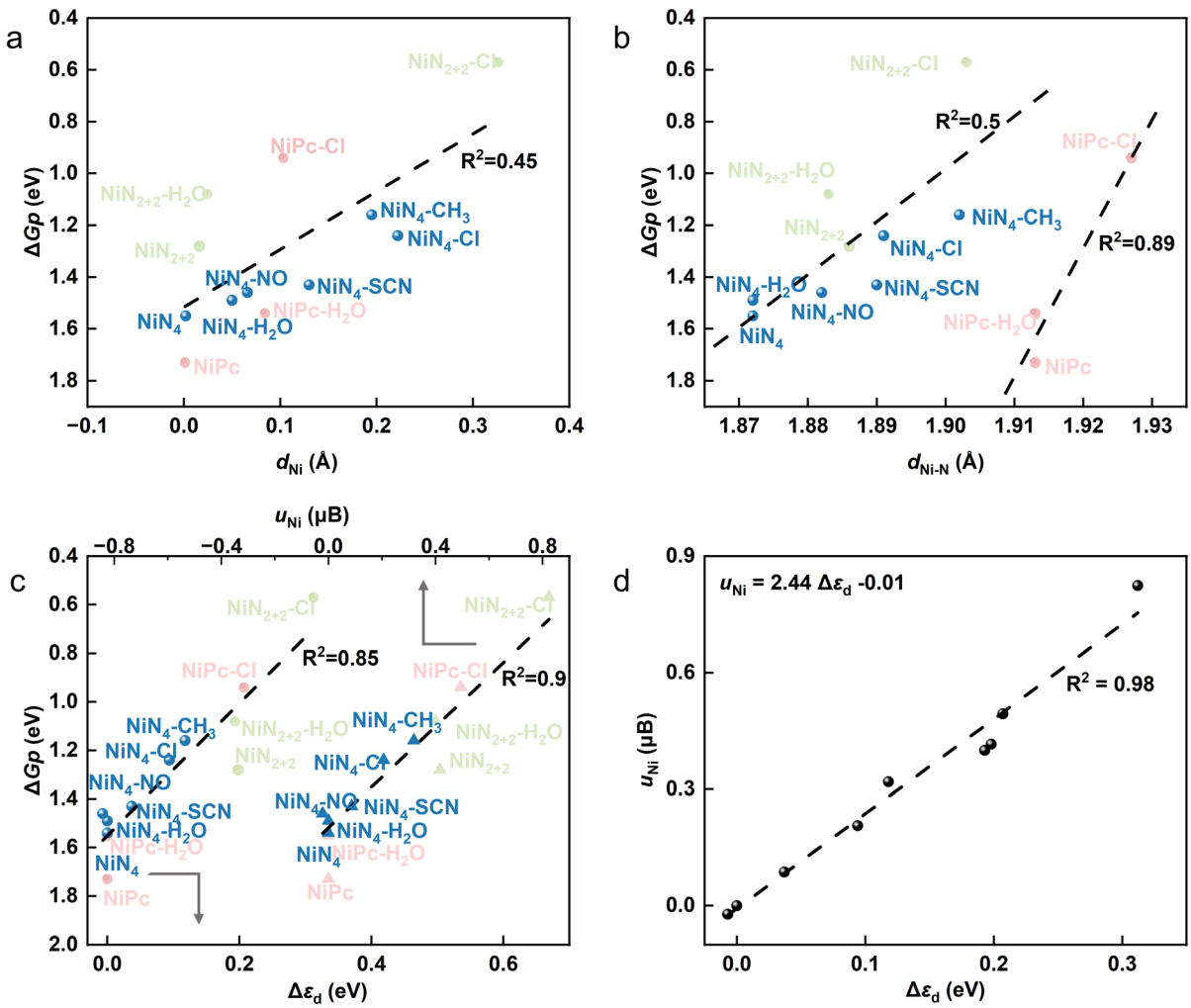

Fig. 5 Universal descriptors for the eCO_2RR activity of Ni–N_4 with various axial ligands. The relationships between ΔG_p and (a) d_{Ni}, (b) d_{Ni-N}, (c) $\Delta\varepsilon_d$, u_{Ni} (the circular symbol represent $\Delta\varepsilon_d$, and the triangular symbol represents u_{Ni}). (d) The relationship between $\Delta\varepsilon_d$ (the difference in the d-band center of Ni between down and up spin) and u_{Ni} (the magnetic moment of Ni atoms).

NiPc (0.207 eV) > NiN_{2+2} (0.114 eV) > NiN_4 (0.094 eV), perfectly matching the trend for the change of ΔG_p induced by Cl axial ligands (NiPc > NiN_{2+2} > NiN_4). Therefore, although the effect of axial ligands on the geometric structure of NiPc is the lowest among all three model structures due to its rigid structure, that on the electronic structures is the highest, resulting in the most significant decrease in ΔG_p for NiPc induced by Cl axial ligands. Since $\Delta\varepsilon_d$ is directly correlated with the electronic asymmetry of Ni–N_4 as discussed above, we can safely conclude that the electronic symmetry breaking, which originates from the geometric symmetry breaking, is the primary factor in enhancing the eCO_2RR activity.

Furthermore, the asymmetric up and down spin electron arrangements of Ni 3d orbitals will cause changes in the magnetic moment of Ni atoms (u_{Ni}), and the linear relationship between $\Delta\varepsilon_d$ and u_{Ni} is shown in Fig. 5d. Therefore, we further investigate the relationship between ΔG_p and u_{Ni}, which also exhibit a good linear correlation: larger the u_{Ni}, lower the ΔG_p (Fig. S13b†). Thus, u_{Ni} and $\Delta\varepsilon_d$ are possible descriptors of the eCO_2RR activity of Ni–N_4-type SACs with axial ligands. The separate linear relationships for NiPc and Ni–N–C systems are unified when using $\Delta\varepsilon_d$ and u_{Ni} as descriptors since electronic properties circumvent the fundamentally different geometries of NiPc and Ni–N–C.

To demonstrate the universality of the above geometric and electronic descriptors, we further extend axial ligands over NiN_4 from Cl^- to –NO, –SCN, and $-CH_3$, and investigate the relationship between ΔG_p and geometric/electronic parameters (d_{Ni}, d_{Ni-N}, u_{Ni}, $\Delta\varepsilon_d$). The configurations of all elementary steps on NiN_4 models are shown in Fig. S14.† The free energy diagrams indicate that all axial ligands over NiN_4 investigated exhibit reduced ΔG_p, and thus promote the electrocatalytic CO_2RR to CO (Fig. S15, S16 and Table S7†). There are linear correlations between ΔG_p and d_{Ni}, d_{Ni-N}, u_{Ni}, $\Delta\varepsilon_d$ for NiN_4 with various ligands (Fig. S17†), which fit well in the linear lines we have described in Fig. 4a, b and S13† (Fig. 5). Therefore, u_{Ni} and $\Delta\varepsilon_d$ are universal descriptors for evaluating the eCO_2RR activity of Ni–N_4-type SACs with a variety of axial ligands, and, most probably, can be extended to other M–N_4-type SACs. The spin electron rearrangement in M–N_4 SACs induced by axial ligands is the key for boosting eCO_2RR activity.

Conclusions

In summary, we investigated the effect of axial ligand on the eCO_2RR activity of two Ni–N_4-type model catalysts (NiPc and Ni–N–C), and both theoretical and experimental studies demonstrate that Cl axial ligand is beneficial for the eCO_2RR. The Cl axial ligand induces a hybridization state transition of nickel orbital from dsp^2 to d^2sp^3 and, consequently, a rearrangement of spin electrons, accounting for the superior activity of Ni–N_4–Cl for the eCO_2RR. The low energy barrier of PDS for the eCO_2RR exhibits a strong correlation with the geometric (d_{Ni} and d_{Ni-N}) and electronic ($\Delta\varepsilon_d$ and u_{Ni}) parameters of Ni–N_4. Furthermore, we propose the magnetic moment of Ni as a universal descriptor for the eCO_2RR toward CO on Ni–N_4 with various axial ligands (–H_2O, –Cl, –NO, –SCN, and $-CH_3$). Our work provides valuable insights on regulating the geometric configuration and electronic structure of SACs to boost their electrocatalytic activities for various energy and environmental applications.

Data availability

All experimental and computational procedures and associated data are provided in the ESI.†

Author contributions

M. P., K. H., and J. L. conceived the project. M. P. prepared materials, performed measurements and analysed the data. K. H. performed the DFT calculations. X. H. and A. Z. helped with some of the experiments and characterization. All authors discussed the results and commented on the manuscript. M. P., K. H., and J. L. wrote the draft, revised and finalized the manuscript.

Conflicts of interest

There are no conflicts to declare.

Acknowledgements

This work was financially supported by the National Natural Science Foundation of China (22102114).

Notes and references

1 A. S. Hall, Immobilized cations boost acidic CO_2 reduction, *Nat. Catal.*, 2023, **6**, 744–745.
2 M. Jiang, H. Wang, M. Zhu, X. Luo, Y. He, M. Wang, C. Wu, L. Zhang, X. Li, X. Liao, Z. Jiang and Z. Jin, Review on strategies for improving the added value and expanding the scope of CO_2 electroreduction products, *Chem. Soc. Rev.*, 2024, **53**, 5149–5189.
3 B. Rhimi, M. Zhou, Z. Yan, X. Cai and Z. Jiang, Cu-Based Materials for Enhanced C2+ Product Selectivity in Photo-/Electro-Catalytic CO_2 Reduction: Challenges and Prospects, *Nano-Micro Lett.*, 2024, **16**, 64.
4 Y. Y. Birdja, E. Pérez-Gallent, M. C. Figueiredo, A. J. Göttle, F. Calle-Vallejo and M. T. M. Koper, Advances and challenges in understanding the electrocatalytic conversion of carbon dioxide to fuels, *Nat. Energy*, 2019, **4**, 732–745.
5 N. Mohd Adli, W. Shan, S. Hwang, W. Samarakoon, S. Karakalos, Y. Li, D. A. Cullen, D. Su, Z. Feng, G. Wang and G. Wu, Engineering Atomically Dispersed FeN_4 Active Sites for CO_2 Electroreduction, *Angew. Chem., Int. Ed.*, 2021, **60**, 1022–1032.
6 Q. He, D. Liu, J. H. Lee, Y. Liu, Z. Xie, S. Hwang, S. Kattel, L. Song and J. G. Chen, Electrochemical Conversion of CO_2 to Syngas with Controllable CO/H_2 Ratios over Co and Ni Single-Atom Catalysts, *Angew. Chem., Int. Ed.*, 2020, **59**, 3033–3037.

7 P. De Luna, C. Hahn, D. Higgins, S. A. Jaffer, T. F. Jaramillo and E. H. Sargent, What would it take for renewably powered electrosynthesis to displace petrochemical processes?, *Science*, 2019, **364**, eaav3506.

8 F. Li, Y. C. Li, Z. Wang, J. Li, D. H. Nam, Y. Lum, M. Luo, X. Wang, A. Ozden, S.-F. Hung, B. Chen, Y. Wang, J. Wicks, Y. Xu, Y. Li, C. M. Gabardo, C. T. Dinh, Y. Wang, T. T. Zhuang, D. Sinton and E. H. Sargent, Cooperative CO_2-to-ethanol conversion *via* enriched intermediates at molecule–metal catalyst interfaces, *Nat. Catal.*, 2019, **3**, 75–82.

9 X. Wang, J. F. De Araújo, W. Ju, A. Bagger, H. Schmies, S. Kühl, J. Rossmeisl and P. Strasser, Mechanistic reaction pathways of enhanced ethylene yields during electroreduction of CO_2–CO co-feeds on Cu and Cu-tandem electrocatalysts, *Nat. Nanotechnol.*, 2019, **14**, 1063–1070.

10 T. Möller, W. Ju, A. Bagger, X. Wang, F. Luo, T. Ngo Thanh, A. S. Varela, J. Rossmeisl and P. Strasser, Efficient CO_2 to CO electrolysis on solid Ni–N–C catalysts at industrial current densities, *Energy Environ. Sci.*, 2019, **12**, 640–647.

11 S. Jin, Z. Hao, K. Zhang, Z. Yan and J. Chen, Advances and Challenges for the Electrochemical Reduction of CO_2 to CO: From Fundamentals to Industrialization, *Angew. Chem., Int. Ed.*, 2021, **60**, 20627–20648.

12 S. Liang, L. Huang, Y. Gao, Q. Wang and B. Liu, Electrochemical Reduction of CO_2 to CO over Transition Metal/N-Doped Carbon Catalysts: The Active Sites and Reaction Mechanism, *Adv. Sci.*, 2021, **8**, 2102886.

13 Y. Zhu, J. Sokolowski, X. Song, Y. He, Y. Mei and G. Wu, Engineering Local Coordination Environments of Atomically Dispersed and Heteroatom-Coordinated Single Metal Site Electrocatalysts for Clean Energy-Conversion, *Adv. Energy Mater.*, 2020, **10**, 1902844.

14 S. Ren, D. Joulié, D. Salvatore, K. Torbensen, M. Wang, M. Robert and C. P. Berlinguette, Molecular electrocatalysts can mediate fast, selective CO_2 reduction in a flow cell, *Science*, 2019, **365**, 367–369.

15 A. S. Varela, W. Ju, A. Bagger, P. Franco, J. Rossmeisl and P. Strasser, Electrochemical Reduction of CO_2 on Metal-Nitrogen-Doped Carbon Catalysts, *ACS Catal.*, 2019, **9**, 7270–7284.

16 Y. Li, N. M. Adli, W. Shan, M. Wang, M. J. Zachman, S. Hwang, H. Tabassum, S. Karakalos, Z. Feng, G. Wang, Y. C. Li and G. Wu, Atomically dispersed single Ni site catalysts for high-efficiency CO_2 electroreduction at industrial-level current densities, *Energy Environ. Sci.*, 2022, **15**, 2108–2119.

17 Z. Yang, R. Chen, L. Zhang, Y. Li and C. Li, Recent progress in nickel single-atom catalysts for the electroreduction of CO_2 to CO, *Ind. Chem. Mater.*, 2024, **2**, 533–555.

18 J. Bai, Z. Sun, H. Zhang, Y. Lian, Y. Deng, M. Xiang and Y. Su, Modulating the Local Coordination Environment of M–N_x Single-Atom Site for Enhanced Electrocatalytic Oxygen Reduction, *Adv. Funct. Mater.*, 2024, 2417013.

19 R. Wang, L. Zhang, J. Shan, Y. Yang, J. F. Lee, T. Y. Chen, J. Mao, Y. Zhao, L. Yang, Z. Hu and T. Ling, Tuning Fe Spin Moment in Fe–N–C Catalysts to Climb the Activity Volcano *via* a Local Geometric Distortion Strategy, *Adv. Sci.*, 2022, **9**, 2203917.

20 X. Cheng, J. Hu, W. Shang, J. Guo, C. Xin, S. Zhang, S. Song, W. Liu and Y. Shi, Asymmetrically ligated single atomic nickel sites for efficient hydrogen peroxide electrosynthesis, *Nano Res.*, 2024, **17**, 1094–1100.

21 H. B. Yang, S. F. Hung, S. Liu, K. Yuan, S. Miao, L. Zhang, X. Huang, H. Y. Wang, W. Cai, R. Chen, J. Gao, X. Yang, W. Chen, Y. Huang, H. M. Chen, C. M. Li, T. Zhang and B. Liu, Atomically dispersed Ni(i) as the active site for electrochemical CO_2 reduction, *Nat. Energy*, 2018, **3**, 140–147.

22 Z. Li, R. Wu, S. Xiao, Y. Yang, L. Lai, J. S. Chen and Y. Chen, Axial chlorine coordinated iron–nitrogen–carbon single-atom catalysts for efficient electrochemical CO_2 reduction, *Chem. Eng. J.*, 2022, **430**, 132882.

23 S. Ding, J. A. Barr, Q. Shi, Y. Zeng, P. Tieu, Z. Lyu, L. Fang, T. Li, X. Pan, S. P. Beckman, D. Du, H. Lin, J. C. Li, G. Wu and Y. Lin, Engineering Atomic Single Metal–FeN_4 Cl Sites with Enhanced Oxygen-Reduction Activity for High-Performance Proton Exchange Membrane Fuel Cells, *ACS Nano*, 2022, **16**, 15165–15174.

24 S. Wei, R. Yang, Z. Wang, J. Zhang and X. H. Bu, Planar Chlorination Engineering: A Strategy of Completely Breaking the Geometric Symmetry of Fe-N_4 Site for Boosting Oxygen Electroreduction, *Adv. Mater.*, 2024, 2404692.

25 J. X. Peng, W. Yang, Z. Jia, L. Jiao and H. L. Jiang, Axial coordination regulation of MOF-based single-atom Ni catalysts by halogen atoms for enhanced CO_2 electroreduction, *Nano Res.*, 2022, **15**, 10063–10069.

26 Y. Chen, S. Ji, S. Zhao, W. Chen, J. Dong, W.-C. Cheong, R. Shen, X. Wen, L. Zheng, A. I. Rykov, S. Cai, H. Tang, Z. Zhuang, C. Chen, Q. Peng, D. Wang and Y. Li, Enhanced oxygen reduction with single-atomic-site iron catalysts for a zinc–air battery and hydrogen–air fuel cell, *Nat. Commun.*, 2018, **9**, 5422.

27 Y. Han, Y. Wang, R. Xu, W. Chen, L. Zheng, A. Han, Y. Zhu, J. Zhang, H. Zhang, J. Luo, C. Chen, Q. Peng, D. Wang and Y. Li, Electronic structure engineering to boost oxygen reduction activity by controlling the coordination of the central metal, *Energy Environ. Sci.*, 2018, **11**, 2348–2352.

28 K. Mou, Z. Chen, X. Zhang, M. Jiao, X. Zhang, X. Ge, W. Zhang and L. Liu, Highly Efficient Electroreduction of CO_2 on Nickel Single-Atom Catalysts: Atom Trapping and Nitrogen Anchoring, *Small*, 2019, **15**, 1903668.

29 Y. J. Sa, H. Jung, D. Shin, H. Y. Jeong, S. Ringe, H. Kim, Y. J. Hwang and S. H. Joo, Thermal Transformation of Molecular Ni^{2+}–N_4 Sites for Enhanced CO_2 Electroreduction Activity, *ACS Catal.*, 2020, **10**, 10920–10931.

30 J. Yang, Z. Qiu, C. Zhao, W. Wei, W. Chen, Z. Li, Y. Qu, J. Dong, J. Luo, Z. Li and Y. Wu, In Situ Thermal Atomization To Convert Supported Nickel Nanoparticles into Surface-Bound Nickel Single-Atom Catalysts, *Angew. Chem., Int. Ed.*, 2018, **57**, 14095–14100.

31 S. Ji, Y. Mou, H. Liu, X. Lu, Y. Zhang, C. Guo, K. Sun, D. Liu, J. H. Horton, C. Wang, Y. Wang and Z. Li, Manipulating the Electronic Properties of an Fe Single Atom Catalyst *via* Secondary Coordination Sphere Engineering to Provide Enhanced Oxygen Electrocatalytic Activity in Zinc-Air Batteries, *Adv. Mater.*, 2024, **36**, 2410121.

32 S. Chen, X. Li, C. W. Kao, T. Luo, K. Chen, J. Fu, C. Ma, H. Li, M. Li, T. S. Chan and M. Liu, Unveiling the Proton-Feeding Effect in Sulfur-Doped Fe–N–C Single-Atom Catalyst for Enhanced CO_2 Electroreduction, *Angew. Chem., Int. Ed.*, 2022, **61**, e202206233.

33 X. Li, T. Chen, B. Yang and Z. Xiang, Fundamental Understanding of Electronic Structure in FeN_4 Site on Electrocatalytic Activity *via* d_z^2-Orbital-Driven Charge Tuning for Acidic Oxygen Reduction, *Angew. Chem., Int. Ed.*, 2023, **62**, e202215441.

34 J. Li, L. Jiao, E. Wegener, L. L. Richard, E. Liu, A. Zitolo, M. T. Sougrati, S. Mukerjee, Z. Zhao, Y. Huang, F. Yang, S. Zhong, H. Xu, A. J. Kropf, F. Jaouen, D. J. Myers and Q. Jia, Evolution Pathway from Iron Compounds to Fe_1(II)–N_4 Sites through Gas-Phase Iron during Pyrolysis, *J. Am. Chem. Soc.*, 2020, **142**, 1417–1423.

35 M. Li, M. Wang, D. Liu, Y. Pan, S. Liu, K. Sun, Y. Chen, H. Zhu, W. Guo, Y. Li, Z. Cui, B. Liu, Y. Liu and C. Liu, Atomically-dispersed NiN_4–Cl active sites with axial Ni–Cl coordination for accelerating electrocatalytic hydrogen evolution, *J. Mater. Chem. A*, 2022, **10**, 6007–6015.

36 S. Yang, Y. Yu, X. Gao, Z. Zhang and F. Wang, Recent advances in electrocatalysis with phthalocyanines, *Chem. Soc. Rev.*, 2021, **50**, 12985–13011.

37 X. Xie, H. Peng, G. Ma, Z. Lei and Y. Xu, Recent progress in heteroatom doping to modulate the coordination environment of M–N–C catalysts for the oxygen reduction reaction, *Mater. Chem. Front.*, 2023, **7**, 2595–2619.

38 Y. He, Q. Shi, W. Shan, X. Li, A. J. Kropf, E. C. Wegener, J. Wright, S. Karakalos, D. Su, D. A. Cullen, G. Wang, D. J. Myers and G. Wu, Dynamically Unveiling Metal–Nitrogen Coordination during Thermal Activation to Design High-Efficient Atomically Dispersed CoN_4 Active Sites, *Angew. Chem., Int. Ed.*, 2021, **60**, 9516–9526.

39 H. Fei, J. Dong, Y. Feng, C. S. Allen, C. Wan, B. Volosskiy, M. Li, Z. Zhao, Y. Wang, H. Sun, P. An, W. Chen, Z. Guo, C. Lee, D. Chen, I. Shakir, M. Liu, T. Hu, Y. Li, A. I. Kirkland, X. Duan and Y. Huang, General synthesis and definitive structural identification of MN_4C_4 single-atom catalysts with tunable electrocatalytic activities, *Nat. Catal.*, 2018, **1**, 63–72.

40 F. Pan, H. Zhang, K. Liu, D. Cullen, K. More, M. Wang, Z. Feng, G. Wang, G. Wu and Y. Li, Unveiling Active Sites of CO_2 Reduction on Nitrogen-Coordinated and Atomically Dispersed Iron and Cobalt Catalysts, *ACS Catal.*, 2018, **8**, 3116–3122.

41 L. Ding, Q. Xin, X. Zhou, J. Qiao, H. Li and H. Wang, Electrochemical behavior of nanostructured nickel phthalocyanine (NiPc/C) for oxygen reduction reaction in alkaline media, *J. Appl. Electrochem.*, 2013, **43**, 43–51.

42 S. A. Mirshokraee, M. Muhyuddin, N. Pianta, E. Berretti, L. Capozzoli, J. Orsilli, F. D'Acapito, R. Viscardi, A. Cosenza, P. Atanassov, C. Santoro and A. Lavacchi, Ni-Phthalocyanine Derived Electrocatalysts for Oxygen Reduction Reaction and Hydrogen Evolution Reaction: Active Sites Formation and Electrocatalytic Activity, *ACS Catal.*, 2024, **14**, 14524–14538.

43 J. Li, P. Pršlja, T. Shinagawa, A. J. Martín Fernández, F. Krumeich, K. Artyushkova, P. Atanassov, A. Zitolo, Y. Zhou, R. García-Muelas, N. López, J. Pérez-Ramírez and F. Jaouen, Volcano Trend in Electrocatalytic CO_2 Reduction Activity over Atomically Dispersed Metal Sites on Nitrogen-Doped Carbon, *ACS Catal.*, 2019, **9**, 10426–10439.

44 C. C. Hou, H. F. Wang, C. Li and Q. Xu, From metal–organic frameworks to single/dual-atom and cluster metal catalysts for energy applications, *Energy Environ. Sci.*, 2020, **13**, 1658–1693.

45 N. Weidler, J. Schuch, F. Knaus, P. Stenner, S. Hoch, A. Maljusch, R. Schäfer, B. Kaiser and W. Jaegermann, X-ray Photoelectron Spectroscopic Investigation of Plasma-Enhanced Chemical Vapor Deposited NiO_x, $NiO_x(OH)_y$, and $CoNiO_x(OH)_y$: Influence of the Chemical Composition on the Catalytic Activity for the Oxygen Evolution Reaction, *J. Phys. Chem. C.*, 2017, **121**, 6455–6463.

46 S. Vijay, W. Ju, S. Brückner, S. C. Tsang, P. Strasser and K. Chan, Unified mechanistic understanding of CO_2 reduction to CO on transition metal and single atom catalysts, *Nat. Catal.*, 2021, **4**, 1024–1031.

47 S. Liu, H. B. Yang, S. F. Hung, J. Ding, W. Cai, L. Liu, J. Gao, X. Li, X. Ren, Z. Kuang, Y. Huang, T. Zhang and B. Liu, Elucidating the Electrocatalytic CO_2 Reduction Reaction over a Model Single-Atom Nickel Catalyst, *Angew. Chem., Int. Ed.*, 2020, **59**, 798–803.

48 Y. Tuo, W. Liu, Q. Lu, X. Zhang, X. Zhou, Y. Zhou, X. Feng, M. Wu, Z. Wang, D. Chen and J. Zhang, Breaking the scaling relationship *via* lattice expansion of Ag for CO_2 electroreduction over a wide potential window, *AIChE J.*, 2024, **70**, e18365.

49 J. W. Chen, Z. Zhang, H. M. Yan, G. J. Xia, H. Cao and Y. G. Wang, Pseudo-adsorption and long-range redox coupling during oxygen reduction reaction on single atom electrocatalyst, *Nat. Commun.*, 2022, **13**, 1734.

50 S. Yu, Z. Levell, Z. Jiang, X. Zhao and Y. Liu, What Is the Rate-Limiting Step of Oxygen Reduction Reaction on Fe–N–C Catalysts?, *J. Am. Chem. Soc.*, 2023, **145**, 25352–25356.

51 P. Hutchison, P. S. Rice, R. E. Warburton, S. Raugei and S. Hammes-Schiffer, Multilevel Computational Studies Reveal the Importance of Axial Ligand for Oxygen Reduction Reaction on Fe–N–C Materials, *J. Am. Chem. Soc.*, 2022, **144**, 16524–16534.

52 L. Hu, C. Dai, L. Chen, Y. Zhu, Y. Hao, Q. Zhang, L. Gu, X. Feng, S. Yuan, L. Wang and B. Wang, Metal-Triazolate-Framework-Derived FeN_4Cl_1 Single-Atom Catalysts with Hierarchical Porosity for the Oxygen Reduction Reaction, *Angew. Chem., Int. Ed.*, 2021, **60**, 27324–27329.

53 J. Li, S. Ghoshal, W. Liang, M. T. Sougrati, F. Jaouen, B. Halevi, S. McKinney, G. McCool, C. Ma, X. Yuan, Z. F. Ma, S. Mukerjee and Q. Jia, Structural and mechanistic basis for the high activity of Fe–N–C catalysts toward oxygen reduction, *Energy Environ. Sci.*, 2016, **9**, 2418–2432.

54 Y. Cui, C. Ren, Q. Li, C. Ling and J. Wang, Hybridization State Transition under Working Conditions: Activity Origin of Single-Atom Catalysts, *J. Am. Chem. Soc.*, 2024, **146**, 15640–15647.